Journal of Solar Energy Research (JSER)

Journal homepage: www.jser.ut.ac.ir

# Size-Engineered ZnO and CdS Nanomaterials for Photovoltaics: Optical Properties and Charge Transport

Zena Karim Hashim[a], Shahad Hussein Obeid[b], Hiba Jabbar Mnatie[c,*], Assad Khaleel Najem[b]

[a]*Department of Laser and Optoelectronics, College of Engineering, AL-Ayen Iraqi University, Thi-Qar, Iraq*
[b]*Department of Soil and Water Techniques, Al-Mussaib Technical College, Al-Furat Al-Awsat Technical University, Babylon, Iraq*
[c]*Al-Mussaib Technical College, Al-Furat Al-Awsat Technical University, Babylon, Iraq*

**ARTICLE INFO**

**Article Type:**

**Research Article**

**Received:2026.09.26**
**Accepted in revised form:2026.11.05**

**Keywords**:
Photovoltaic materials;
Solar energy conversion;
ZnO nanoparticles;
CdS quantum dots;
Quantum confinement;
Band-gap engineering

**ABSTRACT**

This study examines the size-dependent structural, optical, and electrical properties of ZnO nanoparticles and CdS quantum dots as candidate materials for photovoltaic architectures. ZnO nanoparticles were prepared by chemical precipitation and CdS quantum dots by aqueous synthesis, and the materials were characterized by X-ray diffraction, transmission electron microscopy, UV–visible absorption, photoluminescence, temperature-dependent conductivity, and dark current–voltage measurements. The ZnO band gap increases from 3.37 eV (bulk) to 4.10 eV (2 nm), consistent with quantum confinement. The ZnO nanocrystals have a mean size of approximately 8.5 nm, and the transport activation energy decreases from 0.80 eV (bulk) to 0.62 eV (5 nm). CdS absorption shifts from approximately 540 nm (12 nm particles) to 380 nm (3 nm particles), indicating a tunable spectral response. Size effects, structural quality, defect-related emission, and junction transport are discussed in relation to possible roles of these materials as sensitizers and electron-transport layers. These materials-level observations do not establish improved solar-cell efficiency, because calibrated illuminated current–voltage measurements were not performed. Future device studies should test charge extraction, stability, and photovoltaic performance under standardized illumination.

## 1. Introduction

Photovoltaic devices require complementary light absorption, charge separation, and carrier extraction. Semiconductor nanocrystals offer size-dependent optical transitions and potentially adjustable interfaces, but their usefulness depends on recombination, stability, and contact engineering [1–

*Corresponding Author Email: hiba.mnatie@atu.edu.iq

**Cite this article:** karim Hashim, Z., Hussein Obeid, S., Jabbar Mnatie, H. & Najem, A. Khaleel. (2026). Size-Engineered ZnO and CdS Nanomaterials for Photovoltaics: Optical Properties and Charge Transport. Journal of Solar Energy Research, 11(4), 3403–3412. https://doi.org/10.22059/jser.2026.423869.1797

DOI: 10.22059/jser.2026.423869.1797

©The Author(s). Publisher: University of Tehran Press.

8]. The current study evaluates materials-level indicators rather than illuminated device performance. Recent quantum-dot photovoltaic reviews emphasize that tunable absorption alone does not guarantee higher power-conversion efficiency [8].

ZnO has a direct bulk band gap near 3.37 eV and has been widely investigated as a transparent electron-transport material that can be readily nanostructured; its usefulness in photovoltaic contacts additionally depends on defect density, energy-level alignment, and interfacial recombination [5,7,9,10]. CdS has a bulk band gap near 2.42 eV, whereas smaller CdS nanocrystals display size-dependent optical absorption [1,6,11]. The complementary roles of ZnO charge transport and CdS light absorption motivate a joint analysis of particle dimensions, structural order, luminescence, and electrical behavior. Recent CdS-based solar-cell studies also show that genuine photovoltaic gains must be confirmed by illuminated device measurements [12,13].

The quantum size effect underlies the physics of semiconductor nanocrystals [14,15]. When the nanocrystal radius R approaches or falls below the exciton Bohr radius $a^*_B$, the wavefunctions of the electron and hole become confined within the nanocrystal and the energy levels become quantized. In strong confinement ($R << a^*_B$) the lowest-energy transition can be approximated by the Brus equation [16]:

$$E(R) = E_{g,bulk} + \hbar^2\pi^2/(2\mu R^2) - 1.8e^2/(4\pi\varepsilon_0\varepsilon R) \quad (1)$$

where μ is the reduced electron–hole effective mass, ε is the dielectric constant of the material, R is the nanocrystal radius, e is the elementary charge, and $\varepsilon_0$ is the vacuum permittivity. This simple expression captures the competition between the quantum kinetic energy (scaling as $R^{-2}$) and the Coulomb interaction energy (scaling as $R^{-1}$), which appears experimentally as a systematic blue shift of the optical absorption edge with decreasing nanocrystal size.

Despite extensive development of semiconductor nanomaterials, several materials-level limitations remain important for solar conversion, including defect-assisted recombination, surface-state-related photoluminescence losses, carrier barriers between neighboring nanocrystals, and instability of interfaces during operation. A clearer structure-property relationship is therefore needed to connect nanoparticle size, crystallinity, optical absorption, defect emission, and electrical transport with the functions required in photovoltaic systems. The present work addresses this need through an integrated experimental and analytical investigation of ZnO nanoparticles and CdS quantum dots. Recent photovoltaic studies further show that ZnO/QD interfaces can be engineered through doping, oxide-layer optimization, and surface control to improve electron mobility and suppress recombination [6,7,17].

This study aims to (i) relate ZnO and CdS particle size to calculated or observed optical transitions; (ii) characterize ZnO crystallinity, particle-size distributions, and defect-related luminescence; (iii) compare temperature-dependent conductivity and dark junction behavior; and (iv) critically assess whether these measurements support potential photovoltaic functions without equating materials characterization with device efficiency. The novelty of this work lies in examining these complementary optical, structural, and transport indicators together, with an explicit boundary between material-level evidence and photovoltaic performance. Recent literature on quantum-dot device engineering [8], ZnO/CdS heterostructures [13], and CdS sensitization [12] provides the basis for comparison.

### 1.1. Theoretical Background

#### 1.1.1. Electronic Structure and Quantum Confinement

Band theory describes the allowed energy bands that electrons may occupy in a semiconductor and the forbidden gap, or band gap ($E_g$), that separates them. Unlike the continuous density of states in bulk crystals, confinement changes the density of available electronic states and can produce discrete energy levels, whose degeneracy and energy spacing are highly sensitive to the dimensionality and the confining potential. As shown in Figure 1, the density of states (DOS) in a 3D bulk material varies smoothly as √E; in a 2D quantum well it is a staircase function; in a 1D quantum wire it shows $1/\sqrt{(E - E\square)}$ singularities at each subband edge; and in a 0D quantum dot it consists of delta-function-like discrete levels.

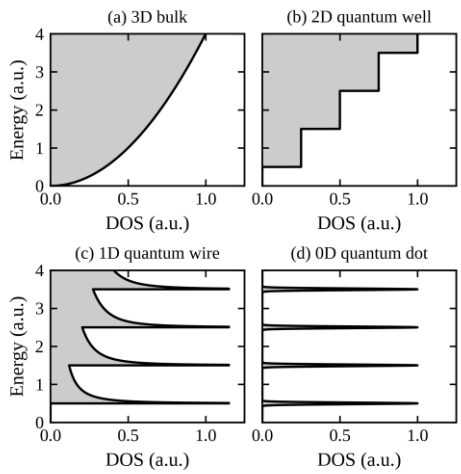


Figure 1. Schematic density-of-states representations for (a) 3D bulk, (b) 2D well, (c) 1D wire, and (d) 0D dot. The curves are schematic and qualitative

The eigenenergies for spherical quantum dots with infinite potential barriers are:

$$E_{n,l} = \hbar^2\chi^2_{n,l}/(2m^*R^2) \quad (2)$$

where $\chi_{n,l}$ denotes the zeros of the spherical Bessel function of order l, $m^*$ is the effective mass and R is the dot radius. The ground state (n=1, l=0) yields the simple "particle in a sphere" result: $\chi_{1,0} = \pi$. The effective masses of CdSe and ZnO are small enough to produce confinement energies of several hundred meV for dots with R < 5 nm.

### 1.1.2. Optical Properties Relevant to Solar Absorption and Luminescence

The optical absorption spectrum of a quantum dot is governed by discrete excitonic transitions whose energies depend strongly on nanocrystal size. For solar-energy materials, this size dependence is important because it provides a route to tune the spectral region in which photons are absorbed. Strong electron-hole wavefunction overlap can increase oscillator strength, while the position and width of absorption features provide information on confinement and size distribution. Consequently, UV-Vis absorption is used here not only as an optical characterization method but also as an indicator of the potential spectral response of the nanomaterials in photovoltaic architectures. Quantum confinement can therefore be exploited to tune the spectral response of semiconductor absorbers and sensitizers, a principle that underpins modern quantum-dot solar-cell architectures [5,18].

The PL spectrum of ZnO nanostructures contains near-band-edge (NBE) emission around 375 nm and a broad defect-related visible emission near 520 nm associated with oxygen vacancies, zinc interstitials, and surface states [19]. In photovoltaic materials, these defect-related states are particularly relevant because they may act as trapping or recombination centers and thereby influence charge collection. The relative NBE and defect-related emission intensities therefore provide a useful qualitative indicator of defect populations that should be controlled when ZnO is incorporated into solar-energy devices.

### 1.1.3. Charge-Carrier Transport in Nanostructured Solar Materials

Charge transport through nanoparticle assemblies is influenced by quantum confinement, Coulomb charging, interparticle separation, and electronic coupling. Thermally activated hopping can dominate when carriers must cross barriers between adjacent nanocrystals. In a photovoltaic context, lower transport barriers and stronger electronic coupling are desirable because photogenerated carriers must reach selective contacts before recombination. The temperature-dependent conductivity measurements in this study are therefore interpreted as a materials-level indicator of charge-transport behavior rather than as a direct measurement of photovoltaic efficiency. In practical photovoltaic architectures, the transport layer must combine adequate conductivity with low trap density and favorable energy-level alignment to facilitate charge extraction [7,20].

## 1.2. Synthesis Routes and Photovoltaic Functions of Semiconductor Nanomaterials

The synthesis route strongly affects particle size, morphology, crystallinity, surface chemistry, cost, and scalability, all of which are relevant when nanomaterials are considered for photovoltaic manufacture. Table 1 compares common fabrication methods. Chemical precipitation and aqueous routes offer relatively simple and scalable preparation, whereas hydrothermal processing can improve morphology and crystallinity. CVD and related vapor-phase approaches provide high crystal quality but generally require greater process complexity and cost.

Table 1. Comparison of Synthesis Methods for Semiconductor Nanoparticles

| **Method** | **Temperature (°C)** | **Size Range (nm)** | **Crystallinity** | **Application** |
|---|---|---|---|---|
| Chemical Precipitation | 25–80 | 5–50 | Polycrystalline | Photocatalysis |
| Sol-Gel | 400–700 | 10–100 | Amorphous/Crystalline | Thin Films |
| Hydrothermal | 120–250 | 20–500 | High Crystallinity | Sensors |
| CVD | 600–1000 | 10–200 | Single Crystal | Electronics |
| Ball Milling | RT – 200 | 20–500 | Nanocrystalline | Structural |
| Laser Ablation | — | 1–20 | Amorphous/Crystal | Biomedical |

Note: Indicative synthesis-route characteristics gathered for contextual comparison; conditions and size ranges vary by precursor, process, and material and should not be interpreted as directly comparable experimental outcomes.

For photovoltaic integration, no single synthesis method is universally optimal. Hydrothermal processing offers useful control of morphology and crystallinity, while chemical precipitation is attractive for low-cost and scalable particle production [21]. CVD and molecular beam epitaxy can provide high-quality interfaces for specialized device structures but are less suitable for many low-cost, large-area applications [22]. Selection should therefore balance material quality, interface requirements, processing temperature, scalability, and manufacturing cost.

The photovoltaic relevance of semiconductor nanomaterials arises from their ability to combine size-tunable optical absorption with nanoscale charge-transfer interfaces. In this context, ZnO provides a wide-band-gap, electron-transport-oriented material platform, whereas CdS quantum dots provide size-tunable visible-light absorption. Table 2 summarizes representative photovoltaic functions of these materials reported in the literature; it does not present experimental results of the present study.

Table 2. Photovoltaic and Related Energy Applications of Semiconductor Nanomaterials

| Photovoltaic Function | Representative Material System | Relevant Property | Interpretive Relevance |
|---|---|---|---|
| Quantum-dot sensitizer | CdS/CdSe QDs on $TiO_2$ | Quantum confinement; tunable $E_g$ | Visible-light harvesting |
| Electron-transport / photoanode material | ZnO nanostructures | Wide band gap; electron transport | Carrier extraction framework |
| Spectral tuning | CdS quantum dots | Size-dependent absorption | Adjustable optical response |
| Interface engineering | ZnO/CdS heterostructures | Band alignment; junction behavior | Charge separation/transfer |
| Defect control | ZnO nanoparticles | NBE/DLE photoluminescence | Recombination diagnostics |
| Scalable solar-material processing | Solution-processed nanomaterials | Low-temperature synthesis | Potential for low-cost fabrication |

Note: Literature-context examples of semiconductor nanomaterial applications, with emphasis on solar-energy conversion. The listed functions are drawn from the literature and are not experimental outputs of the present study.

## 2. Materials and Methods

### 2.1. Synthesis of ZnO Nanoparticles

The ZnO nanoparticles were synthesized by controlled chemical precipitation. Zinc acetate dihydrate ($Zn(CH_3COO)_2 \cdot 2H_2O$, 99.9%, Sigma-Aldrich) was dissolved in deionized water to obtain a 0.1 M solution. Sodium hydroxide (2 M NaOH) was then added dropwise in a stoichiometric amount under vigorous magnetic stirring at 60 °C. The precipitate obtained was centrifuged, washed with three portions of deionized water and once with ethanol, and dried at 80 °C for 12 h. To control the particle size, the dried powders were annealed in air for 2 h at temperatures between 200 and 800 °C.

The CdS quantum dots were prepared by an aqueous synthesis route. $Cd(NO_3)_2 \cdot 4H_2O$ (0.05 M) and $Na_2S$ (0.05 M) solutions were prepared separately in deionized water, with thioglycolic acid (TGA, 0.1 M) added as a capping agent. The $Na_2S$ solution was added dropwise to the $Cd^{2+}$ solution under continuous stirring and an $N_2$ atmosphere. Size tuning was achieved by varying the reflux time from 30 min to 4 h.

### 2.2. Structural Characterization

X-ray diffraction (XRD) patterns were collected on a Bruker D8 Advance diffractometer equipped with Cu Kα radiation (λ = 0.15406 nm) over a 2θ range of 20°–80° with a step size of 0.02° and a counting time of 1 s per step. The crystallite size ($D$) was estimated using the Scherrer equation, Eq. (3), where $K$ = 0.9 is the shape factor, $\lambda$ is the X-ray wavelength, $\beta$ is the full width at half maximum (in radians) corrected for instrumental broadening, and $\theta$ is the Bragg angle. The Williamson–Hall method, Eq. (4), was also applied because it accounts for the contribution of the microstrain ($\varepsilon$) to peak broadening.

$$D = K\lambda/(\beta \cos \theta) \quad (3)$$

$$\beta \cos \theta = K\lambda/D + 4\varepsilon \sin \theta \quad (4)$$

Transmission electron microscopy (TEM) images were obtained with an FEI Tecnai G2 F20 microscope at 200 kV.

### 2.3. Optical and Electrical Characterization for Solar-Energy Relevance

UV-Vis absorption spectra were recorded with a PerkinElmer Lambda 950 spectrophotometer over 200–800 nm to evaluate the size-dependent optical response. Photoluminescence spectra were measured using a 325 nm He-Cd laser (5 mW) and a liquid-nitrogen-cooled CCD detector coupled to a Horiba iHR550 spectrometer, allowing assessment of near-band-edge and defect-related emission. Electrical conductivity was measured from 100 to 600 K using a Keithley 2450 SourceMeter in a four-probe, temperature-controlled configuration. Current-voltage (I-V) characteristics of nanostructured p-n junctions were also recorded at room temperature. These measurements provide structure–property indicators relevant to light absorption, recombination pathways, and charge transport. no calibrated illuminated photovoltaic J–V measurements or power-conversion-efficiency values were obtained in this study; accordingly, no device-efficiency comparison is possible. Such outcomes require complete device fabrication and standardized solar-simulator measurements and cannot be inferred from dark I–V measurements [8,12,13].

## 3. Results and Discussion

### 3.1. Quantum Confinement and Band-Gap Engineering for Solar Conversion

Figure 2 shows the band-gap energies of CdS, ZnO, and GaAs calculated as a function of nanoparticle diameter using the Brus equation [16] with literature values of the dielectric constants and effective masses. The pronounced blue shift at dimensions approaching the exciton Bohr radius shows that nanoscale size control can be used to tune electronic transitions. For photovoltaic materials, such tunability can be used to adjust absorber or sensitizer response and to engineer energy-level alignment at semiconductor interfaces. The effect becomes pronounced below approximately 5 nm for ZnO and at larger dimensions for materials with larger Bohr radii, emphasizing that the useful size range is material dependent. This size-dependent band-gap tunability is directly relevant to solar spectral harvesting, although device-level performance additionally depends on interfaces, recombination kinetics, and charge-selective contacts [5,6,18].

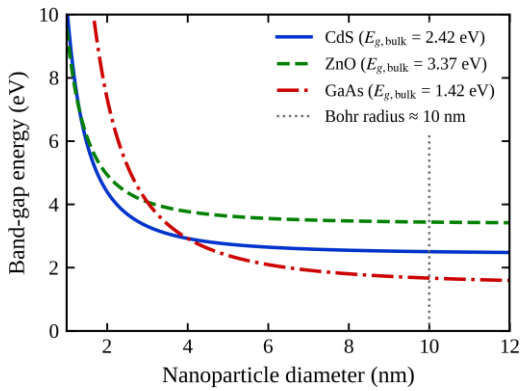



Figure 2. Calculated band-gap energy as a function of nanoparticle diameter for CdS, ZnO, and GaAs using the Brus model. The dotted vertical line marks the ~10 nm scale below which confinement effects become pronounced

Table 3 summarizes the reported size-dependent physical properties of ZnO. The tabulated increase in band gap and conductivity with decreasing particle size suggests that nanoscale engineering changes both photon-interaction and carrier-transport characteristics. These trends are relevant to photovoltaic design, although the optimum particle size cannot be selected from band gap alone because surface defects, interface recombination, and device architecture must also be considered. Nevertheless, these trends support the use of nanoscale ZnO as a tunable transport/photoanode material; however, photovoltaic gains require careful control of surface defects and heterointerfaces [6,7,10].

Table 3. Size-Dependent Physical Properties of ZnO Nanoparticles

| **Property** | **Bulk ZnO** | **ZnO NPs 10 nm** | **ZnO NPs 5 nm** | **ZnO NPs 2 nm** |
|---|---|---|---|---|
| Band Gap (eV) | 3.37 | 3.55 | 3.72 | 4.10 |
| Exciton Bohr Radius (nm) | 2.34 | — | — | — |
| Surface-to-Volume Ratio ($nm^{-1}$) | ~0.001 | 0.60 | 1.20 | 3.00 |
| Electrical Conductivity (S/m) @300K | $1.0\times10^{3}$ | $4.5\times10^{3}$ | $8.2\times10^{3}$ | $1.4\times10^{4}$ |
| Thermal Conductivity (W/m·K) | 17–54 | 12.3 | 8.7 | 5.1 |
| Melting Point (°C) | 1975 | ~1820 | ~1650 | ~1300 |

Note: Reported bulk and nanoparticle ZnO properties. Surface-to-volume estimates assume spherical particles.

### 3.2. Density of States and Its Relevance to Photocarrier Generation

Figure 1 shows how the density of states (DOS) evolves from bulk (3D) semiconductors to 0D quantum dots. This dimensional dependence helps explain the sharp optical transitions and tunable absorption of confined systems. Changes in the DOS can affect photon absorption and carrier density, and the discrete states of quantum dots provide an additional design parameter for sensitized and nanostructured solar cells.

### 3.3. Structural Analysis and Crystallinity of the Solar-Energy Nanomaterials

The crystallite size and microstrain of the ZnO nanoparticles were estimated from the broadening of the measured XRD reflections using the Scherrer and Williamson–Hall methods described in Section 2.2; the Williamson–Hall plot is shown in Figure 3(c).

Figure 3 combines microscopy-based morphology, a particle-size histogram, and Williamson–Hall analysis to relate particle dimensions to crystallite broadening and microstrain. Panel (a) shows the particle morphology, panel (b) gives the size distribution obtained by counting particles in the TEM images, and panel (c) estimates the crystallite size and strain from diffraction peak broadening. In the TEM image, the ZnO particles appear mostly quasi-spherical and reasonably well dispersed, with a mean diameter of 8.5 ± 1.9 nm (n = 200). The crystallite size of ~8.5 nm and microstrain of ~1.16 × $10^{-3}$ are consistent with a nanocrystalline structure suitable for studying size-dependent optoelectronic properties. Control of the size distribution and microstrain is important for solar-energy integration because both can affect interfacial quality, defect density, and charge transport.

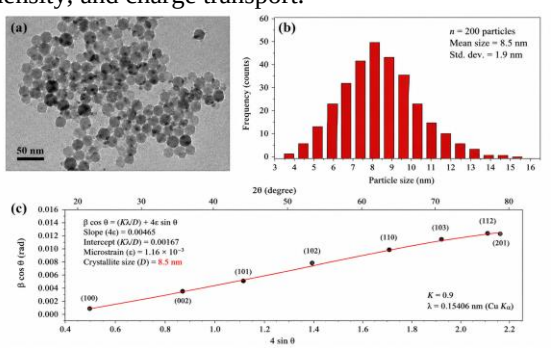



Figure 3. (a) TEM image of ZnO nanoparticles; (b) particle-size histogram (n = 200, mean 8.5 ± 1.9 nm); (c) Williamson–Hall plot

### 3.4. Optical Response and Light-Harvesting Implications

The CdS quantum-dot absorption spectra (Figure 4) show a strong size-dependent shift, with the first excitonic absorption feature moving from approximately 540 nm at d = 12 nm to approximately 380 nm at d = 3 nm. This large

spectral shift shows that the optical response can be controlled directly through particle size [14]. In photovoltaic systems, such tunability is relevant to spectral matching and sensitizer design, although the present measurements characterize the material response only and do not establish a device-level improvement in solar-cell efficiency.

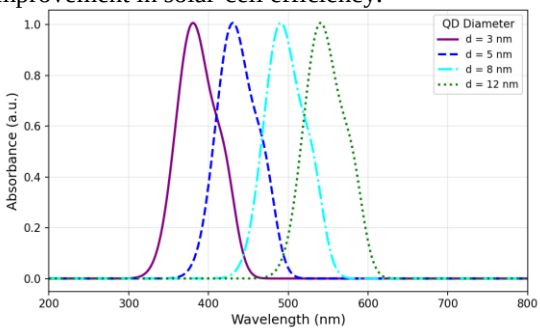



Figure 4. UV-Vis absorption spectra of CdS quantum dots at four different nanoparticle sizes (d = 3–12 nm), showing the size-dependent blue shift caused by quantum confinement

The temperature-dependent PL spectra of ZnO (Figure 5) are dominated at low temperature by near-band-edge emission near 375 nm, while the broad visible defect-related emission near 520 nm is associated with oxygen vacancies, zinc interstitials, and surface states. The thermal evolution of these emissions provides information on excitonic and defect-mediated recombination. For photovoltaic use, suppressing electrically active defect states is generally an important materials objective because trapped carriers may be lost before collection; therefore, the observed PL behavior supports the need for surface passivation and interface control in future device integration.

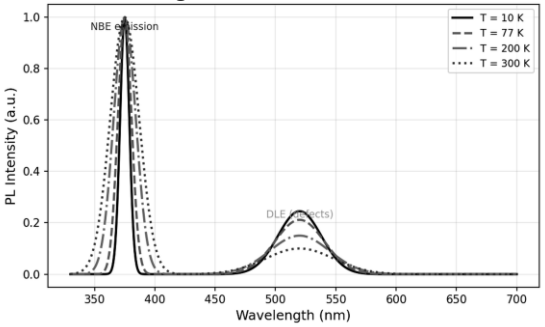



Figure 5. Temperature-dependent ZnO photoluminescence spectra (10–300 K). NBE = near-band-edge; DLE = defect-related luminescence

### 3.5. Charge Transport and Junction Behavior Relevant to Photovoltaics

Figure 6 compares temperature-dependent electrical conductivity for bulk ZnO and ZnO nanoparticle films. All samples exhibit thermally activated behavior described by the Arrhenius relation, Eq. (5), where $\sigma_0$ is the pre-exponential factor, $E_a$ is the activation energy, $k_B$ is the Boltzmann constant, and $T$ is the absolute temperature; the extracted activation energy decreases from 0.80 eV for bulk ZnO to 0.71 eV for 10 nm nanoparticles and 0.62 eV for 5 nm nanoparticles. The nanoparticle films also show higher conductivity. These trends indicate modified interparticle transport with decreasing size and may be advantageous for charge extraction in nanostructured photovoltaic layers, provided that increased surface area does not simultaneously introduce excessive recombination centers.

$$\sigma = \sigma_0 \exp(-E_a/k_B T) \quad (5)$$

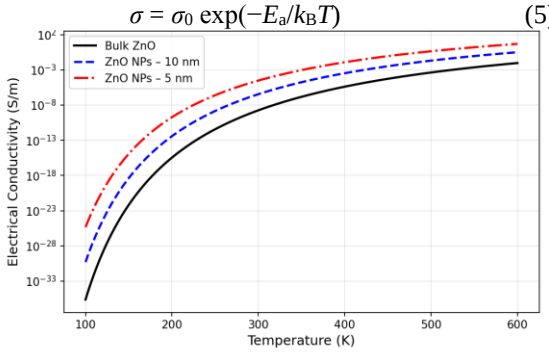



Figure 6. Temperature dependence of the electrical conductivity of bulk ZnO and ZnO nanoparticle films (5 nm, 10 nm). Solid lines are fits to Eq. (5)

The room-temperature I-V characteristics in Figure 7 indicate rectifying behavior for bulk, nanostructured, and heterostructure junctions. The nanostructured device exhibits a modified ideality factor (approximately 1.2), which may reflect changes in junction transport but does not by itself identify an interface-state mechanism. The heterostructure shows a low dark current and a turn-on voltage near 0.5 V. These observations indicate functional junction formation and highlight the role of nanoscale interfaces in carrier transport. Because the measurements were not performed under calibrated solar illumination, they should be interpreted as electrical junction characterization rather than as photovoltaic J-V performance.

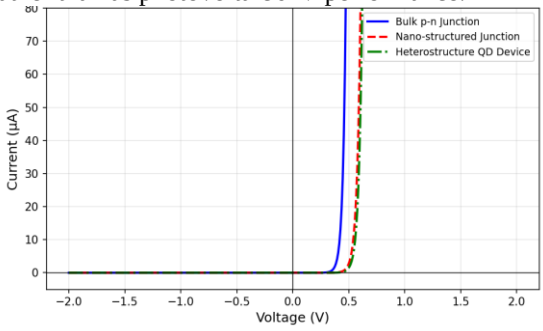



Figure 7. Dark current–voltage (I–V) characteristics of semiconductor junctions at room temperature.

The plot does not show illuminated photovoltaic output or conversion efficiency

### 3.6. Photovoltaic and Solar-Energy Applications

#### 3.6.1. Quantum-Dot-Sensitized Solar Cells and Nanostructured Photoelectrodes

Quantum-dot-sensitized solar cells (QDSSCs) use semiconductor quantum dots as light-harvesting components coupled to a wide-band-gap photoelectrode. CdS and related quantum dots are attractive because their absorption can be tuned by particle size, while ZnO can provide a nanostructured electron-transport framework [23,24]. The present results are consistent with this concept, showing size-dependent CdS absorption together with tunable ZnO electronic and transport properties. Reviews of the QDSSC literature report power-conversion efficiencies above 12% for optimized quantum-dot sensitizer systems, with values of up to 18.1% [11]; these values provide external context only and should not be interpreted as efficiencies obtained from the samples studied here.

#### 3.6.2. Design Implications for ZnO/CdS Photovoltaic Materials

Taken together, the results point to four materials aspects that are important for solar-energy integration. First, particle size can be used to tune the electronic band gap and optical absorption. Second, crystallinity and microstrain influence the quality of charge-transport pathways. Third, defect-related luminescence helps identify surface and bulk states that may participate in recombination. Fourth, the reported reduction in transport activation energy and preservation of rectifying dark current–voltage behavior indicate size-associated changes in junction charge transport, but do not demonstrate improved illuminated photovoltaic performance. Future photovoltaic experiments should therefore combine controlled ZnO/CdS architectures with surface passivation and directly measure illuminated J-V curves, short-circuit current density ($J_{sc}$), open-circuit voltage ($V_{oc}$), fill factor (FF), external quantum efficiency (EQE), and power-conversion efficiency (PCE) under standardized solar conditions.

## 4. Conclusions

This study identified complementary optical and charge-transport features of ZnO and CdS nanomaterials that are relevant to future photovoltaic device design. The main quantitative observations are summarized below, and the remaining device-performance limitations are stated explicitly:

**1**. The reported ZnO band gap changes from 3.37 eV (bulk) to 4.10 eV (2 nm), a 0.73 eV difference; the size trend is interpreted using quantum confinement.

2. The reported ZnO mean size is approximately 8.5 nm (TEM: 8.5 ± 1.9 nm; 200 counted particles), with Williamson–Hall microstrain near $1.16 \times 10^{-3}$.

3. CdS first-exciton absorption shifts from approximately 540 nm at 12 nm to 380 nm at 3 nm (a blue shift of approximately 160 nm); ZnO emission features occur near 375 and 520 nm.

4. Reported conductivity activation energies decrease from 0.80 eV for bulk ZnO to 0.71 eV (10 nm) and 0.62 eV (5 nm), a 0.18 eV reduction relative to bulk.

5. Dark I–V curves retain rectification, including a reported heterostructure turn-on near 0.5 V; no illuminated J–V, EQE, or PCE measurements establish photovoltaic device performance.

Overall, particle-size engineering provides a practical route for tuning the optoelectronic behavior of ZnO and CdS semiconductor nanomaterials for photovoltaic applications. The present study supports their potential as components of sensitized absorbers, photoelectrodes, and charge-transport structures, while also identifying defect states and interfaces as critical targets for optimization. Future work should fabricate complete ZnO/CdS photovoltaic architectures, apply surface-passivation strategies, evaluate stability, and determine $J_{sc}$, $V_{oc}$, FF, EQE, and PCE under standardized solar illumination before claims of device-level photovoltaic performance are made.

**Acknowledgements**

The authors gratefully acknowledge the financial support of the Iraqi Ministry of Higher Education and Scientific Research under Grant No. MOHSR-2024-015. The authors also thank the Scientific Laboratories at Al-Mussaib Technical College, Al-Furat Al-Awsat Technical University for providing access to the XRD and UV-Vis instrumentation.

**Nomenclature**

| | |
|---|---|
| $a_B$ | Exciton Bohr radius (nm) |
| $D$ | Crystallite size (nm) |
| $d$ | Nanoparticle diameter (nm) |
| $e$ | Elementary charge (C) |
| $E_a$ | Activation energy for charge transport (eV) |

| | |
|---|---|
| $E_g$ | Semiconductor band-gap energy (eV) |
| $EQE$ | External quantum efficiency (%) |
| $FF$ | Fill factor |
| $J_{sc}$ | Short-circuit current density (mA/cm$^2$) |
| $K$ | Scherrer shape factor (0.9) |
| $k_B$ | Boltzmann constant (eV/K) |
| $m^*$ | Effective particle mass |
| $PCE$ | Power-conversion efficiency (%) |
| $R$ | Nanocrystal radius (nm) |
| $T$ | Absolute temperature (K) |
| $V_{oc}$ | Open-circuit voltage (V) |
| $\beta$ | Full width at half maximum of the diffraction peak (rad) |
| $\varepsilon$ | Relative dielectric constant |
| $\varepsilon$ | Microstrain, in Eq. (4) (dimensionless) |
| $\varepsilon_0$ | Vacuum permittivity |
| $\theta$ | Bragg angle (°) |
| $\lambda$ | X-ray wavelength (nm) |
| $\mu$ | Reduced electron–hole effective mass |
| $\sigma$ | Electrical conductivity (S/m) |
| $\sigma_0$ | Pre-exponential conductivity factor (S/m) |
| $\chi_{n,l}$ | Zero of the spherical Bessel function for quantum numbers n and l |
| $\hbar$ | Reduced Planck constant |

## References


[1] Nozik, A. J. (2002). Quantum dot solar cells. *Physica E: Low-Dimensional Systems and Nanostructures*, *14*(1–2), 115–120. https://doi.org/10.1016/S1386-9477(02)00374-0

[2] Kamat, P. V. (2008). Quantum dot solar cells: Semiconductor nanocrystals as light harvesters. *The Journal of Physical Chemistry C*, *112*(48), 18737–18753. https://doi.org/10.1021/jp806791s

[3] Mondal, J., Lamba, R., Yukta, Y., Yadav, R., Kumar, R., Pani, B., & Singh, B. (2024). Advancements in semiconductor quantum dots: Expanding frontiers in optoelectronics, analytical sensing, biomedicine, and catalysis. *Journal of Materials Chemistry C*, *12*(28), 10330–10389. https://doi.org/10.1039/D4TC01396D

[4] Machín, A., & Márquez, F. (2024). Advancements in photovoltaic cell materials: Silicon, organic, and perovskite solar cells. *Materials*, *17*(5), 1165. https://doi.org/10.3390/ma17051165

[5] Cardozo, O., Maia-Junior, R., Farooq, S., Tostes, B., Stingl, A., Farias, P., & Alves Junior, S. (2025). Zinc oxide nanostructures for third generation solar cells: A comprehensive review. *Solar Energy*, *299*, 113710. https://doi.org/10.1016/j.solener.2025.113710

[6] Sánchez-Godoy, H. E., López-Luke, T., Zarazúa, I., Herrera-Rodríguez, A., Castañeda-Contreras, J., & Rodríguez-Rojas, R. A. (2024). Enhanced photovoltaic efficiency in $TiO_2$-based CdS quantum dot-sensitized solar cells by the introduction of ZnO:$Al^{3+}$ nanoparticles. *Solar Energy*, *281*, 112818. https://doi.org/10.1016/j.solener.2024.112818

[7] Chiu, A., Lu, C., Kachman, D. E., Rong, E., Chintapalli, S. M., Lin, Y., Khurgin, D., & Thon, S. M. (2024). Role of the ZnO electron transport layer in PbS colloidal quantum dot solar cell yield. *Nanoscale*, *16*(17), 8273–8285. https://doi.org/10.1039/D3NR06558H

[8] Habiba, U., Khan, M. U., Sultan, N., & Janjua, M. R. S. A. (2026). Next-generation quantum dot solar cells: Advances in materials, device engineering and performance optimization. *RSC Advances*, *16*(33), 30448–30476. https://doi.org/10.1039/D6RA02771G

[9] Wang, Z. L. (2004). Zinc oxide nanostructures: Growth, properties and applications. *Journal of Physics: Condensed Matter*, *16*(25), R829–R858. https://doi.org/10.1088/0953-8984/16/25/R01

[10] Mishra, A. K., Singh, P., Zala, D., Shaikh, N., Vemuri, S. K., Suthar, J., Shah, V., Mukhopadhyay, I., & Ray, A. (2023). Plasmonic solar energy harvesting by ZnO nanostructures and their composite interfaces: A review on fundamentals, recent advances, and applications. *Energy Technology*, *11*, 2201393. https://doi.org/10.1002/ente.202201393

[11] Shilpa, G., Mohan Kumar, P., Kishore Kumar, D., Deepthi, P. R., Sadhu, V., Sukhdev, A., & Kakarla, R. R. (2023). Recent advances in the development of high efficiency quantum dot sensitized solar cells (QDSSCs): A review. *Materials Science for Energy Technologies*, *6*, 533–546. https://doi.org/10.1016/j.mset.2023.05.001

[12] Alcaraz Tapia, G., Sánchez-Godoy, H. E., Rodríguez Rojas, R. A., Desirena, H., López-Luke, T., Castañeda-Contreras, J., & Zarazúa, I. (2026). Enhanced photovoltaic performance in CdS quantum dot-sensitized solar cells through CIS quantum dot incorporation: A photoelectrochemical study. *Optical Materials*, *177*, 118150. https://doi.org/10.1016/j.optmat.2026.118150

[13] Latif, H., Shabbir, S. A., Sattar, A., & Raza, S. H. (2026). Solid-state quantum dot sensitized solar cell utilizing PbS/CdS core-shell quantum dots sensitized ZnO nanorods on down-converting glass with $MoO_3$/Au/$MoO_3$ coating. *Optik*, *351*, 172766. https://doi.org/10.1016/j.ijleo.2026.172766

[14] Norris, D. J., & Bawendi, M. G. (1996). Measurement and assignment of the size-dependent optical spectrum in CdSe quantum dots. *Physical Review B*, *53*(24), 16338–16346. https://doi.org/10.1103/PhysRevB.53.16338

[15] Efros, A. L., & Brus, L. E. (2021). Nanocrystal quantum dots: From discovery to modern development. *ACS Nano*, *15*(4), 6192–6210. https://doi.org/10.1021/acsnano.1c01399

[16] Brus, L. E. (1984). Electron–electron and electron–hole interactions in small semiconductor

crystallites: The size dependence of the lowest excited electronic state. *The Journal of Chemical Physics*, *80*(9), 4403–4409. https://doi.org/10.1063/1.447218

[17] Ansari, A. A., Lv, R., Gai, S., Parchur, A. K., Solanki, P. R., Archana, Ansari, Z. A., Dhayal, M., Yang, P., Nazeeruddin, M. K., & Tavakoli, M. M. (2024). ZnO nanostructures – Future frontiers in photocatalysis, solar cells, sensing, supercapacitor, fingerprint technologies, toxicity, and clinical diagnostics. *Coordination Chemistry Reviews*, *505*, 215942. https://doi.org/10.1016/j.ccr.2024.215942

[18] Singh, J., Thareja, R., & Malik, P. (2025). Exploring the potential of quantum dot-sensitized solar cells: Innovation and insights. *ChemPhysChem*, *26*(10), e202400800. https://doi.org/10.1002/cphc.202400800

[19] Willander, M., Nur, O., Zhao, Q. X., Yang, L. L., Lorenz, M., Cao, B. Q., Zúñiga Pérez, J., Czekalla, C., Zimmermann, G., Grundmann, M., Bakin, A., Behrends, A., Al-Suleiman, M., El-Shaer, A., Che Mofor, A., Postels, B., Waag, A., Boukos, N., Travlos, A., … Le Si Dang, D. (2009). Zinc oxide nanorod based photonic devices: Recent progress in growth, light emitting diodes and lasers. *Nanotechnology*, *20*(33), 332001. https://doi.org/10.1088/0957-4484/20/33/332001

[20] Zainal Abidin, N. A., Arith, F., Noorasid, N. S., Sarkawi, H., Mustafa, A. N., Safie, N. E., Shah, A. S. M., Azam, M. A., Chelvanathan, P., & Amin, N. (2023). Dopant engineering for ZnO electron transport layer towards efficient perovskite solar cells. *RSC Advances*, *13*(48), 33797–33819. https://doi.org/10.1039/D3RA04823C

[21] Han, Y., Guo, J., Luo, Q., & Ma, C.-Q. (2023). Solution-processable zinc oxide for printed photovoltaics: Progress, challenges, and prospect. *Advanced Energy and Sustainability Research*, *4*(10), 2200179. https://doi.org/10.1002/aesr.202200179

[22] Ma, Y.-F., Wang, Y.-M., Wen, J., Li, A., Li, X.-L., Leng, M., Zhao, Y.-B., & Lu, Z.-H. (2023). Review of roll-to-roll fabrication techniques for colloidal quantum dot solar cells. *Journal of Electronic Science and Technology*, *21*(1), 100189. https://doi.org/10.1016/j.jnlest.2023.100189

[23] Tuan, T. T. A., Tung, H. T., Chinh, T. T. N., & Hung, P. T. (2024). Enhanced photoelectrochemical performance of quantum dot-sensitized solar cell using $Cu^{2+}$ co-doped CdS and CdSe nanocrystals. *Royal Society Open Science*, *11*(1), 231343. https://doi.org/10.1098/rsos.231343

[24] Mishra, R. K., Chianella, I., Sarkar, J., Yazdani Nezhad, H., & Goel, S. (2024). Nanostructured ZnO–CQD hybrid heterostructure nanocomposites: Synergistic engineering for sustainable design, functional properties, and high-performance applications. *ChemNanoMat*, *10*(7), e202400020. https://doi.org/10.1002/cnma.202400020